Combined MEG and EEG suggest a limbic source network of the P3 in retrosplenial cortex, insula, and hippocampus

Diptyajit Das[a], Matti S. Hämäläinen[b], Andrew R. Dykstra[c], Andre Rupp[a], and Alexander Gutschalk[a,]*

[a] *Department of Neurology, Ruprecht-Karls-Universität Heidelberg, Im Neuenheimer Feld 400,*

69120 Heidelberg, Germany

[b] *Department of Neuroscience and Biomedical Engineering, Aalto University School of Science, Espoo, Finland*

[c] *School of Communication Sciences and Disorders, University of Central Florida, Orlando, FL, USA*

*** Corresponding author:**

E-mail address: Alexander.Gutschalk@med.uni-heidelberg.de (A. Gutschalk).

Abstract

Intracranial P3 activity in the hippocampus is a robust phenomenon, but it remains debated if this activity contributes to the extracranial P3. A second limbic P3 source was recently suggested in the retro-splenial cortex based on source analysis and fMRI. The present study tested if these sources could be confirmed by source modeling of a new data set. Combined magneto- and electroencephalography signals were recorded during a visual oddball paradigm. Observers were instructed to respond to rare targets of a deviant shape and ignore rare non-targets of a deviant color. Source analysis was based on noise-normalized minimum norm estimates in an individual, MRI-based cortical source space. Source analysis showed a strong P3 source in retrosplenial cortex. Further sources were observed in insular cortex and medial temporal lobe. The source configuration was similar for rare target and non-target stimuli. Simulations and further analyses show that the source in retrosplenial cortex is strongly attenuated in magnetoencephalography, whereas the source in medial temporal lobe and insula contribute to both recording modalities. These data further support a P3 generator in retrosplenial cortex. Moreover, previously suggested generators in insula and medial temporal lobe, most likely in the hippocampus, are confirmed. In summary, the source configuration presented here suggests that the P3 is confined to limbic circuits.

Keywords: P300, source analysis, hippocampus, retrosplenial cortex

Abbreviations:

AC, Auditory cortex; aMCC, anterior midcingulate cortex; dSPM, dynamic statistical parametric mapping; EEG, electroencephalography; MEG, magnetoencephalography; MTL, medial temporal lobe; ROI, regions of interest; RSC, retro-splenial cortex; S1, primary somatosensory cortex.

Introduction

The P3, also known as P300, is an evoked response observed for active target detection or salient, rare events (Polich, 2007; Verleger, 2020) and is one of the most studied electrophysiological brain responses in cognitive neuroscience (Bledowski et al., 2004; Das et al., 2024; Halgren et al., 1995b, 1995a; Mulert et al., 2004). Using direct intracranial recordings from human epilepsy patients, P3-like activity was first found in the hippocampus (Halgren et al., 1980). Because resection of the hippocampus in such patients did not reduce the scalp P3, it was later suggested that the hippocampal P3 was generated in a closed source that is not the source of the P3 recorded with scalp electroencephalography (EEG) and with a maximum at electrode location Pz (Johnson, 1988; Onofrj et al., 1992). Later, magnetoencephalography (MEG) studies that used dipole source analysis reported that the main generator of the P3 in was in the medial temporal lobe (MTL), most likely in the hippocampus (Basile et al., 1997; Rogers et al., 1993; Tarkka et al., 1995). Others proposed instead that several regions in the parietal and frontal cortex are more likely sources of the P3 (Bledowski et al., 2004; Halgren et al., 1995b, 1995a; Mulert et al., 2004), and the latter interpretation was most widely accepted until today, whereas the role of hippocampus remained unclear.

By applying distributed source analysis to combined MEG and EEG (M/EEG) data obtained with an auditory oddball paradigm, Das et al (Das et al., 2024) recently suggested that the main generator of the P3 is the retro-splenial cortex (RSC). RSC activity was similarly observed in fMRI for the same participants and could well explain the maximum of the P3 response in electrode location Pz in further simulation studies. While this finding would well explain that the parietal midline P3 was not reduced by loss of the medial temporal lobe, it does not necessarily imply that the hippocampal P3 cannot be observed in other electrode or sensor locations outside of the head. Moreover, the RSC is tightly connected with the hippocampus (Kobayashi and Amaral, 2007, 2003), raising interesting interpretations of the P3 at a functional level. MTL activity was also observed when mapping the P3 with distributed source estimation, but the authors could not rule out that MTL activity could be caused by mislocalized source-estimate spread from the insular or auditory cortex (Das et al., 2024). The point-spread of such source models mainly depends on the proximity and alignment (source orientation) of dipolar sources in nearby brain regions, a well-known problem when interpreting the analysis of bioelectrical signals in MEG and EEG (Hämäläinen et al., 1993; Hauk et al., 2022). Leakage from other regions is important to consider in light of the fact that another generator of the P3 has been suggested in the insular cortex (Bledowski et al., 2004; Citherlet et al., 2020; Das et al., 2024) and because activity in the auditory cortex in the P3 latency range is readily evoked by auditory oddballs even without a task (Kretzschmar and Gutschalk, 2010).

Finally, it is important to note that there are two variants of the P3, which have been referred to as P3a and P3b in the past: P3b is evoked by task-relevant target stimuli and shows the typical centro-parietal maximum at Pz in EEG (Hillyard et al., 1971). P3a has been reported in response to rare non-target stimuli (Squires et al., 1975) with a somewhat more anterior, central maximum at Cz. It has been suggested that novel stimuli generate yet another P3 component (Courchesne et al., 1975), but most authors today think that the novelty P3 and the P3a are the same evoked components (Polich, 2007). While lesions of the medial temporal lobe did not affect the P3b, as outlined above, the P3a has been shown to be strongly reduced in patients with unilateral lesions of the medial temporal lobe, while leaving an intact P3b topography (Knight, 1996).

The present study sought to further explore the generator structure of the P3 based on the following three hypotheses: First, we tested if distributed source analysis would indicate a P3 generator in the MTL. To this end, we used a visual instead of an auditory oddball paradigm, which anatomically mitigates spread from auditory cortex to potential sources in the hippocampus and insula. To further mitigate possible spread to these regions from auditory cortex, white noise was used to mask the sounds of button presses in response to detected targets. Second, we tested if the source in RSC – suggested by the previous auditory study (Das et al., 2024) – could be confirmed for the visual stimulus modality. Third, we similarly probed the source in insular cortex. Additionally, a distractor was added to the stimulus paradigm to explore how the source

analysis differs between target and distractor-evoked P3 responses. Further analyses were performed to explore how the MEG and EEG results compare for both, source analysis and simulations.

Materials and Methods

Participants

A group size of 20 participants was expected to provide reliable results, since a previous study had shown converging group-level source maps with 10 or more data sets, already. Accordingly, a total of 22 individuals (11 female, 11 male) between 24 and 61 years of age (mean ± standard deviation = 30.9 ± 8 years) participated in the study. None reported a history of neurological or ophthalmological disorders other than myopia. 20 participants were right-handed and two left-handed. All participants had either normal or corrected-to-normal vision, and none were color blind. Participants were students or employees recruited on campus, with no current neurological or psychiatric health issues or medication. Data from three participants were excluded due to measurement artifacts (n = 2) or co-registration errors (n = 1). Each participant gave written informed consent prior to participation, and the study was approved by the ethical council of the medical faculty at Heidelberg University.

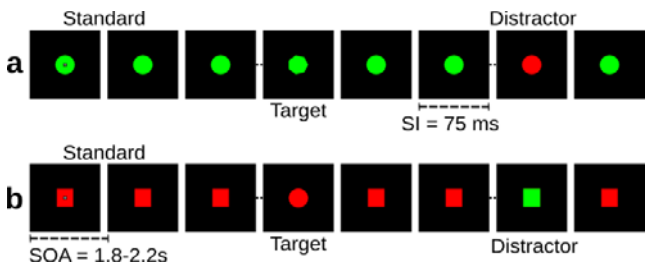

Figure 1: Overview of the experimental design. (a) Stimulus sequence in variant 1: green circles were presented as the standard stimuli, red circles as distractor stimuli, and green heptagons served as targets. (b) Stimulus sequence in variant 2: red squares were presented as standards, red circles as targets, and the green squares were distractors. Stimuli in both variants were shown in the middle of the screen against a black background. Each stimulus lasted for a stimulus interval (SI) of 75 ms and was presented with a stimulus-onset asynchrony (SOA) of 1.8 - 2.2 s. As soon as a target stimulus appeared on the screen, participants were asked to identify it by using their right index finger to click a response button.

Stimuli and experimental design

A visual oddball paradigm (Figure 1) was utilized to evoke a P3 response. The paradigm consists of two similar experimental task conditions, which were used with the intention to reduce habituation in the relatively long recording session, and which were presented in the same order to all participants. In task 1, green circles (visual angle: 1.31° x 1.31°; radius = 3.5 cm), green heptagons (visual angle: 1.31° x 1.31°; 7 sides, side length = cm, and apothem = 3.5 cm), and red circles (visual angle: 1.31° x 1.31°; radius = 3.5 cm) were presented as standard, target, and distractor stimuli. In Task 2, the standard stimuli were red squares (visual angle: 1.31° x 1.31°; radius = 3.5 cm), the target stimuli were red circles (visual angle: 1.31° x 1.31°; radius = 3.5 cm), and the distractors were green squares (visual angle: 1.31° x 1.31°; radius = 3.5 cm). All stimuli were presented with the same luminans and a refresh rate of 120 Hz in a dimly lighted environment (6.5 Lux). For each task, a total of 668 trials were presented, with the probabilities of standard, target, and distractor being 0.79, 0.12, and 0.9, respectively. Each stimulus lasted for 75 milliseconds and was presented at a regular interval of 2 s, with a jitter of ± 200 ms.

All stimuli were created using Psychtoolbox-3 and presented on a black background with a resolution of 1920*1080 pixels. Images were back-projected on a transparent screen mounted in a window of a magnetically shielded room (height = 31 cm and width = 35 cm), 152 cm in front of the participants, with a BenQ TK700STi projector placed outside of the magnetically shielded room. The fixation cross was initially positioned precisely at the center of the screen. Participants were instructed to maintain their gaze on the fixation cross for the duration of each run. The participants were not instructed about the presence

of distractor stimuli in the task. They were specifically told to identify only the target stimuli by clicking a response button using their right index finger as soon as a target stimulus appeared on the screen. A short break was provided in between the two tasks. Prior to each task condition, a practice session consisting of 20 trials without any distractors was undertaken to allow participants to become familiar with the task. During the experiment, constant Gaussian white noise was presented at 80 dB SPL to mask the sound produced by pressing the response button. The sound was delivered binaurally using ER-3 earphones (Etymotics Research, Elk Grove Village, IL, USA) with foam tips.

Data acquisition

The MEG recordings were conducted in a room equipped with four layers of magnetic shielding (IMEDCO AG, Hägendorf, Switzerland) during regular working hours. The recordings were performed using a Neuromag-122 whole-head system (MEGIN OY, Helsinki, Finland) comprising 61 dual-channel planar first-order gradiometers. The EEG data were obtained using a 63-channel equidistant cap (Easycap, Herrsching, Germany) where the electrodes extend far down from the low cheeks until below the inion. Cz was used as a reference electrode, and the impedances of all electrodes were kept below 3 kΩ. A bipolar electrode (near the clavicle) was utilized to record the ECG (electrocardiogram) and was later used as a marker to remove cardiac artifacts from the brain signals. EEG signals were amplified using two 32-channel Neuroscan amplifiers (Abbotsford, Victoria, Australia) and sampled together with the MEG at a frequency of 1000 Hz. The positions of MEG head coils, EEG electrodes, and some additional head-shape points (~80 in total) were digitized together using the Polhemus Isotrack II digitizer (Colchester, Vermont, USA). Four head-position indicator coils were additionally digitized and used to acquire the participant's head position relative to the MEG sensors.

Anatomical 3D T1 (MPRAGE) and T2 (FLAIR) MRI scans were obtained using a 3-T Siemens Magnetom Prisma scanner (Siemens Medical Systems, Erlangen, Germany) to create an accurate boundary-element head model. MPRAGE parameters included a field of view (FOV) of 256×256×192 voxels (voxel size = 1 mm^3), repetition time (TR) = 1570 ms, echo time (TE) = 2.67 ms, inversion time (TI) = 900 ms, and flip angle = 9°. FLAIR parameters included a FOV of 192×256×25 voxels (voxel size = 0.9×0.9×5.5 mm), TR = 8500 ms, TE = 135 ms, TI = 2400 ms, and flip angle = 170°.

Data processing

Preprocessing and source estimation of MEG and EEG signals were carried out using MNE-Python (Gramfort, 2013). The raw data for each participant was visually inspected. Flat and noisy EEG channels were interpolated using the spherical spline method (Perrin et al., 1989). The oversampled temporal projection (OTP) technique was used to remove flux jumps from MEG channels (Larson and Taulu, 2018). The data were then filtered using a zero-phase finite-impulse-response (FIR) bandpass filter (0.5–30 Hz), and the EEG data were re-referenced into the average reference. Next, the FastICA algorithm was used to remove cardiac artifacts and eye blinks (Hyvarinen, 1999). Epochs were obtained using time intervals of 100 ms pre-stimulus to 1 s post-stimulus. Three stimulus-driven epoch conditions were constructed during this stage: standard, target, and distractor. A separate time window of 500 ms pre-stimulus and 500 ms post-stimulus was considered to create epochs to track the response-locked brain activity. Epochs involving missed trials and false alarms were excluded from the analysis. An automatic data-driven 'autoreject' method (Jas et al., 2017) was used to repair or exclude artifact-contaminated epochs. Prior to performing source analysis, the number of epochs across experimental conditions was equalized and averaged to produce separate evoked signals per condition.

Source localization

A combined M/EEG source estimation was performed using the linear L2 minimum-norm estimator (MNE) (Hämäläinen and Ilmoniemi, 1994; Molins et al., 2008) with noise normalization. Cortical surfaces (white and pial) for each participant were reconstructed from high-resolution T1-weighted structural MRI scans using FreeSurfer software (Dale et al., 1999; Fischl, 2012). Participant-specific source spaces were created by placing at least 10,242 sources (dipoles) per hemisphere at

the gray-white matter boundary, with an average spacing of 3.1 mm between the neighboring sources. Sources within the corpus callosum, thalamus, and lateral ventricle wall were omitted using Human Connectome Project (HCP) parcellation (Glasser et al., 2016), as these regions do not include any part of the cortex.

For inverse modeling, three-compartment boundary-element models (BEM) were used to create participant-specific, realistic head models (Hamalainen and Sarvas, 1989). The conductivities of the brain, skull, and skin were assumed to be 0.3 S/m, 0.006 S/m, and 0.3 S/m, respectively. Sources were assigned a loose orientation constraint (parameter value of 0.2), indicating a nearly perpendicular orientation to the cortical surface, which has been shown to improve source localization (Lin et al., 2006). A noise-covariance matrix was computed using the shrinkage technique from the 100-ms long pre-stimulus interval (Engemann and Gramfort, 2015). Dynamic statistical parametric mapping (dSPM) was then based on noise normalized MNE (Dale et al., 2000). Estimates from individuals were morphed onto the FreeSurfer template brain (fsaverage), and a grand-average dSPM source estimate was created by averaging across participants.

For tasks 1 and 2, separate dSPMs were computed to account for different head positions during MEG recordings. Since these separate dSPMs produced very similar results, an average across tasks was performed to create a single dSPM solution. Later, this solution was used to show significant brain activity maps ($p < 0.01$). To extract local source waveforms, several regions of interest (ROI) were defined. A detailed description of ROI definition is provided in our previous auditory study (Das et al., 2024). In total, 5 bilateral ROIs were used, including the left and right insula, somatosensory hand area (S1), medial temporal lobe (MTL), retrosplenial cortex (RSC), and anterior midcingulate cortex (aMCC). Insula and RSC were directly adopted from the previous auditory study. The MTL ROI was not part of the previous analysis and was therefore newly defined. The ROI was restricted to the upper bank of the parahippocampal gyrus, directly opposite the hippocampus. The S1 and aMCC ROIs were adjusted slightly in comparison to the auditory study in order to more accurately include the activation peak of the current data set. Further information regarding this adjustment can be found in the results section. Why the activation peaks did not match between the visual and auditory studies remains unclear; one possible explanation for S1 could be the utilization of different response devices. For each experimental condition, dSPM-based source time-courses for these ROIs were calculated separately by averaging the activity across all sources within each ROI using the 'mean-flip' method implemented in MNE-Python (Gramfort, 2013). This method compensates for signal cancellation by correcting the polarities of the dipoles in comparison to the average orientation produced by all dipoles for a given ROI. This process was carried out for each participant separately before producing a grand-average source time-course across the participants. Because of the restriction of our ROIs to one bank of a sulcus or gyrus, the application of the mean-flip procedure produced only minor effects and did not alter our conclusions.

Peak-latency analysis was performed on the ROI-based source time-courses to compare peak latencies for target versus distractor conditions across participants. For this procedure, the evoked signals were band-pass filtered at 1–8 Hz using a zero-phase-shift FIR filter. Peak latencies for individual ROIs were estimated within a time window between 300-700 ms after stimulus onset. Afterwards, two-sample t-tests were carried out to compare peak latencies between target and distractor P3 within each ROI. The p-values of the tests were corrected for multiple comparisons using a Bonferroni correction with an alpha level of 0.05, and only the corrected p-values ($p<0.05$) are reported.

Source leakage and sensitivity matrix

Spatial source leakage is inherent for MEG and EEG source signals due to their limited spatial resolution and the non-uniqueness of the inverse problem (Sarvas, 1987). The degree to which source leakage varies depends mostly on the type of source estimation method being used and how it is affected by sensor configurations, source depth, and source orientation (Hauk et al., 2022).

In this study, point-spread functions (PSFs) were computed to quantitatively characterize source leakage activation among the selected ROIs for the dSPM method. Initially, the dSPM-based resolution matrix for each participant was computed

independently. PSFs for each ROI were then extracted as the columns of the resolution matrix and summarized by calculating the mean across dipoles (vertices) within the given ROI. Then, a group average of ROI-specific PSFs across participants was performed. Finally, an absolute Pearson correlation test was performed between the leakage activation (grand-PSFs) of one ROI and the rest of the ROIs to determine how the point source activity from one ROI would spread to other ROIs. In this case, correlation values range from 0 to 1, where 1 signifies complete leakage and 0 signifies no leakage.

In addition, the sensitivity matrix of the MEG and EEG sensor types was calculated to investigate source visibility, i.e., how the sensitivity of the sources within these ROIs would vary with respect to sensor type. First, the sensitivity matrix for each sensor type was computed by extracting the columns corresponding to normal components from the gain matrix for each participant. This sensitivity matrix was then morphed onto the fsaverage brain atlas, enabling the computation of a grand-sensitivity matrix across all subjects. Following this, normalization of the grand-sensitivity matrix was performed by dividing it by its maximum value. The normalized matrix was then reduced to an ROI-specific sensitivity matrix, with the values of left and right hemisphere ROIs being averaged to represent a bilateral source sensitivity matrix for individual ROIs. Sensitivity values range from 0 to 1, where 1 signifies maximum source sensitivity and 0 represents no sensitivity with respect to the sensor type.

Cortical source simulations

The cortical source simulation model was implemented in a manner consistent with our previous auditory study (Das et al., 2024). For each participant, bilateral anatomically constrained sources were simulated based on the selected ROIs. All dipolar sources within each ROI were activated using a half-sinusoidal wave timeseries with a base frequency of 5 Hz, chosen to approximate a P3-like waveform. The scaling of the source currents for dipoles was adjusted to ensure that the absolute mean value of all dipoles within an ROI equaled 25 nAm at the peak activity, corresponding to the time instant with the absolute maximum amplitude. This ensures uniform source strength across ROIs, regardless of variations in their sizes. The polarity of the simulated source time-course was also adjusted with the observed polarity in the source analysis. Finally, dipoles within the left and right hemisphere ROIs were combined to create a bilateral source. This process yielded four bilateral sources: insula, MTL, RSC, and aMCC, with the exception of the S1 source, where only left-hemisphere dipoles were considered to replicate contralateral, response-hand-specific brain activity. The simulated sources were then transformed back to the electrode/sensor space to produce simulated evoked signals by multiplying the simulated time-series of the sources by the gain matrix. The individual participants' noise-covariance matrices derived from the M/EEG data were scaled to a total of 200 averages and added to simulated evoked signals to replicate realistic sensor noise. For each participant's dataset, cortical dSPM source estimates were re-computed from these simulated evoked signals. A grand dSPM source estimate across all participants was then calculated at the peak activity to represent significant brain activation maps ($p < 0.01$), following the same approach used for the analysis of the recorded data.

The original, 122-chanel gradiometer MEG data were transformed into 61 virtual magnetometers using MNE-Python (Gramfort, 2013), to equalize the number of MEG sensors and EEG electrodes for the least-squares procedure described in Section 0. Spatial maps of EEG and MEG (magnetometers) were then computed at the peak of the simulated evoked signals for each individual dataset and then averaged across all subjects to produce grand-average spatial maps for both modalities.

P3 pattern analysis using simulated sources

The activation patterns of anatomically constrained simulated sources were linearly combined to explain the P3 peak activation in experimental M/EEG data for targets and distractors. The aim of this procedure is to find a simulated activation pattern such that, when the simulated sources are multiplied by their respective weights and linearly combined, they explain the actual P3 pattern in a least-squares sense. A multiple linear regression approach (Haufe et al., 2014) was utilized here to optimize the weights from the simulated sources. This model can be expressed as:

(1)

(2)

Where, is the predicted simulated P3 pattern; is the actual P3 pattern; is the activation pattern of the ith simulated sources; is the weight of the ith simulated source; and are the optimal weights.

First, evoked M/EEG data were band-pass filtered at 1–8 Hz using a zero-phase FIR filter, and a search window of 300–700 ms was used for reliable P3 peak detection. P3 activation peaks were then extracted from Pz across participants to compute a grand average P3 pattern. Later, the grand-average P3 distribution is used as the target pattern (dependent variable) in the regression model. Five simulated sources (insula, S1, MTL, aMCC, and RSC) were considered as the input variables (input features). Since EEG and MEG data consist of different units, z-scored standardization was performed across individual sensor types utilizing a 50-ms pre-stimulus time interval. We performed this step for both input and actual target variables, ensuring that we could compute latent weights by combining EEG and MEG data, as long as the data remained z-scored (unit-less). To achieve better uniformity, virtual magnetometer data (61 channels) are considered instead of gradiometers for MEG to maintain a similar number of MEG sensors and EEG electrodes. A multi-collinearity test was also performed to establish linear independence across input variables (simulated sources). A variance-inflation factor of 5 was observed across simulated sources during the test, meaning all the simulated sources were fairly independent from each other. Finally, to quantify the performance of the model, residual variance was calculated from the score of the model, which was calculated between the actual and predicted P3 pattern. This step was separately performed for EEG and MEG data. The optimized latent weights were multiplied by the source strength (25 nAm) of the simulated sources to provide a rough estimate of the source strength, leading to the generation of the actual P3 peak pattern in MEG and EEG. All the relevant parameter information for this analysis is provided in **Table 1**.

Results

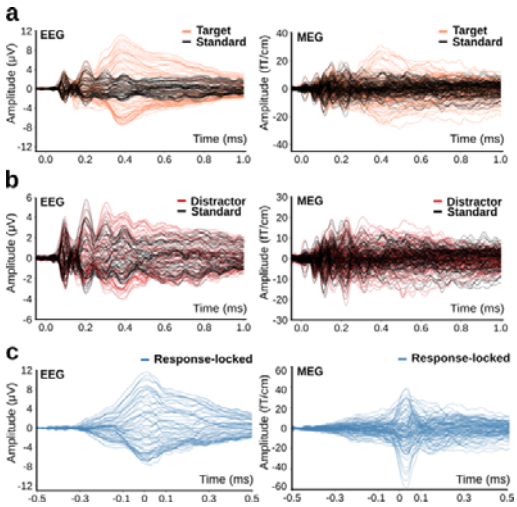

Figure 2: Grand-average evoked signals for EEG and MEG (N=19). (a) Stimulus-locked evoked signals for EEG (left) and MEG (right) for targets (coral) and standards (black). Only the targets evoke prominent P3 activity, which occurs mostly in the 350–450 ms time range. (b) The evoked responses for distractors (red) and standards (black) are shown for EEG (left) and MEG (right). There is only a relatively weak distractor P3 observed in the range of 300 – 500 ms. Note the different amplitude scaling in a and b. (c) Evoked signals for detected targets, averaged by the button press. The somatosensory feedback is evident in MEG (right), which shows a very pronounced and rapidly growing response after the button press. In contrast, EEG (left) is dominated by a progressively increasing signal prior to the initiation of the button press.

The data are based on a visual oddball paradigm with two non-standard stimuli. The targets were of the same color as the standards but of a different shape, and the distractors were of a different color. Participants were instructed to press a response button for the target stimuli, and to ignore the non-standard distractor stimuli. Two variants of the stimulus paradigm were used (Figure 1) with the intention to reduce response habituation. The hit rates for the two variants were similar and not significantly different across participants, with hit rates of 99.8 ± 0.67% in variant 1 and 99.3 ± 0.71% in variant 2 (mean ± standard deviation). The reaction times were 423 ± 49 ms and 425 ± 60 ms (mean ± standard deviation) in variants 1 and 2, respectively. As the separate analyses of the M/EEG data were also highly similar, the two variants were combined for the analysis presented below, to yield a better signal-to-noise ratio. The separate results for task 1 and task 2 are shown in supplement (Figure S1).

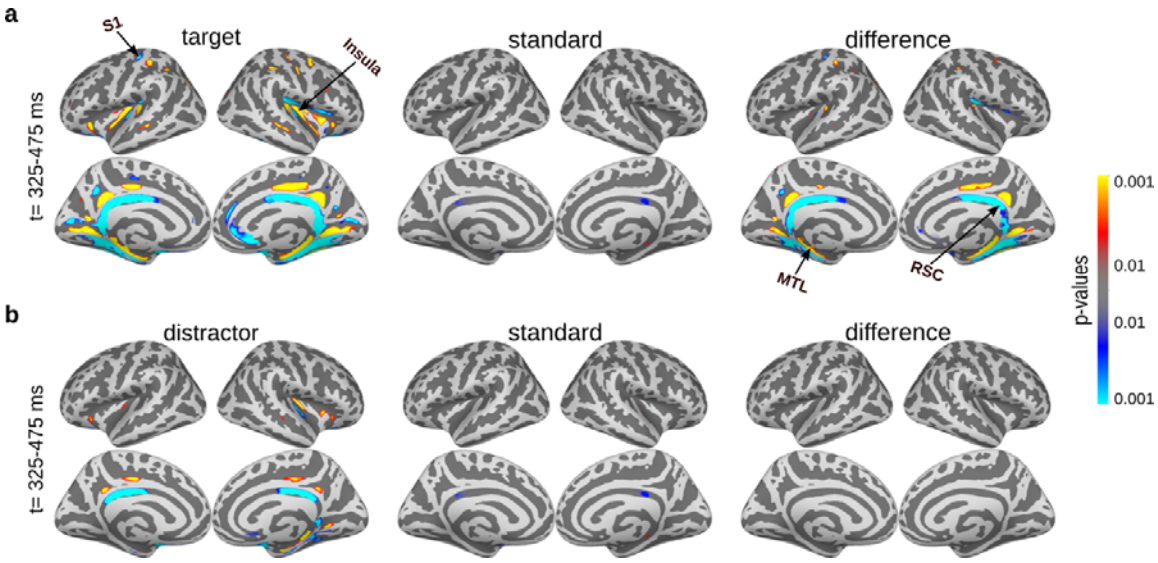

Figure 3: Grand-average dSPM activation maps for combined M/EEG (N=19). (a) Combined M/EEG dSPM maps (p<0.01) for targets (left), standards (middle), and the contrast between targets minus standards (right) in the time window 325–475 ms after stimulus onset. (b) dSPM maps for distractor stimuli, similarly arranged. The number of trials were equalized between targets, distractors, and standards prior to source estimation. Highlighted brain regions include medial temporal lobe (MTL), retrosplenial cortex (RSC), primary somatosensory cortex (S1), and insula.

In the grand average scalp-EEG waveforms (Figure 2a, b; left panel), four subsequent peaks are observed in response to the standard stimuli, with response latencies around 100, 200, 300, and 390 ms. The target response (Figure 2a) was instead dominated by a strong P3 with a response latency of 396 ± 50 ms (mean ± standard deviation, measured at electrode Pz). The third and fourth peaks were also enhanced for the distractor stimulus (Figure 2b), but much less than for the target stimuli. We consider the fourth peak with a mean latency of 383 ± 80 ms (measured at electrode Pz) as the distractor P3 in this case. Similar responses were observed in the MEG sensor-level waveforms (Figure 2; right panel), but with somewhat less distinct P3 compared to EEG. The waveforms of the evoked response averaged relative to the time of the button responses (Figure 2c) showed peaks shortly after the button press, which were more broad-based in EEG (left) compared to MEG (right).

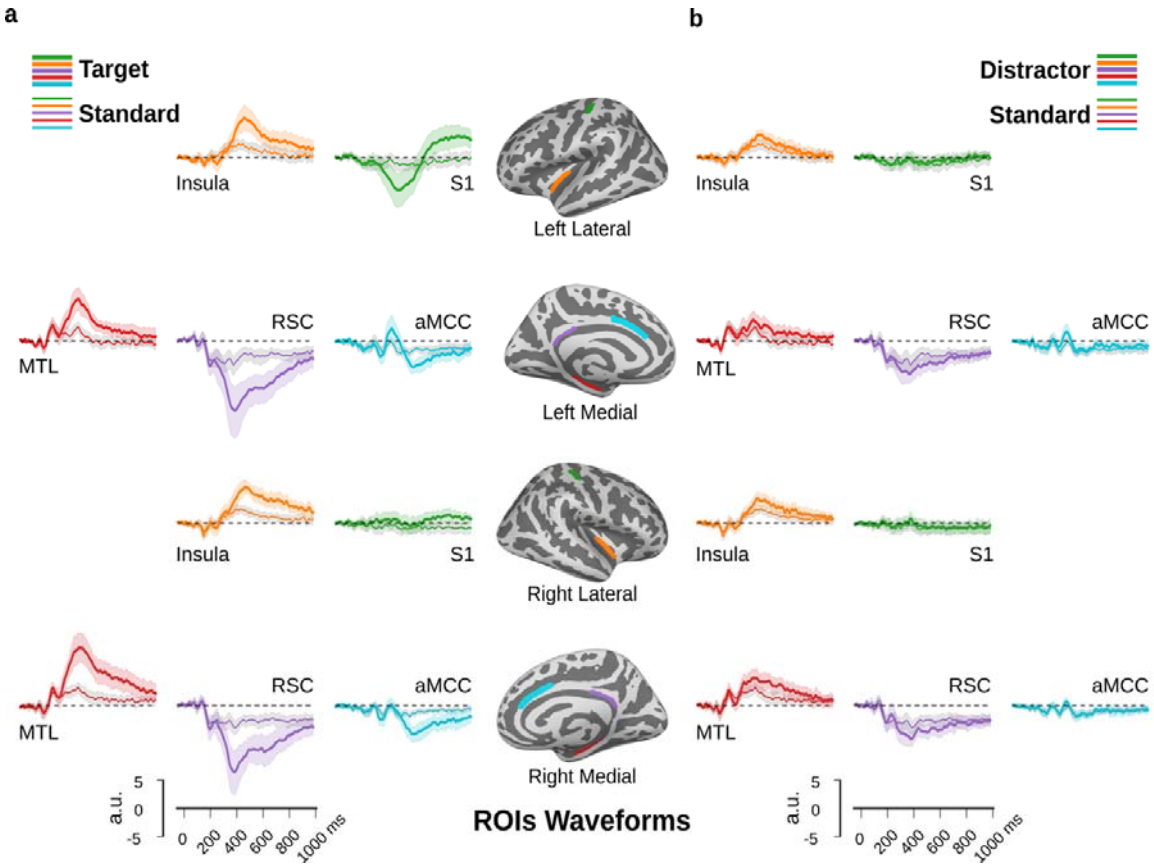

Figure 4: ROIs based M/EEG source waveforms for target, standard and distractor (N=19). (a) M/EEG source waveforms extracted from dSPM estimates across participants for targets (thick lines) and standards (thin lines). The ROIs are plotted in the inflated fsaverage brain (middle column). The same color code is used to represent each ROI and its corresponding source waveform. The ROIs include the insula, primary somatosensory cortex (S1), medial temporal lobe (MTL), retrosplenial cortex (RSC), and anterior midcingulate cortex (aMCC). The shaded areas represent the 95% confidence intervals, calculated using a non-parametric bootstrap method. (b) Similar arrangement of source waveforms but for distractors (thick lines) and standards (thin lines

Grand-average dSPM source maps of the combined M/EEG were then calculated in a time window of 325–475 ms after stimulus onset, covering the P3 peak across participants. The dSPM maps for the target stimuli (Figure 3a) first showed surface-negative polarity in the RSC, accompanied by surface positive activity in two spots along the (dorsal) posterior cingulate gyrus (PCC). As has been shown before (Das et al., 2024) and is also demonstrated further below, such pairs of positive and negative-polarity on opposite sides of a gyrus are typically observed in dSPM maps with sources on one side of a gyrus. A combination of positive- and negative-polarity activity was also observed in MTL along the parahippocampal gyrus, with positive-going activity in the sulcus directly opposite to the hippocampus - the subiculum - and negative-going activity on the opposite side of the parahippocampal gyrus. At the border between the MTL and RSC clusters, activity extends into the calcarine fissure. Some midline activity was finally observed in the right anterior cingulate gyrus (ACC). On the cortical convexity, the largest cluster of activity mapped is located in the insular cortex in both hemispheres. Less prominent spots of activity are mapped to the central region and the superior temporal sulcus. Mapping the activity evoked by standards in the same time range and with the same cutoff reveals almost no activity. Accordingly, the difference between targets and standards (Figure 3a) reveals similar activity patterns in RSC and along the parahippocampal gyrus, as observed for the targets. In contrast, the insular activity is not clearly observed in the difference maps. Similar source analysis results were obtained with the LCVM beamformer (Figure S2a) or sLORETA (Figure S2b) in alternative to dSPM. The maps for distractor stimuli are shown in the same arrangement in Figure 3b: Distractor maps show consistent activity in the bilateral RSC and MTL, along the right parahippocampal gyrus in the midline. Some spots of activity in the convexity are observed

in insular cortex, also more prominently on the right. Neither of these activities are observed in the standard maps nor in the difference maps.

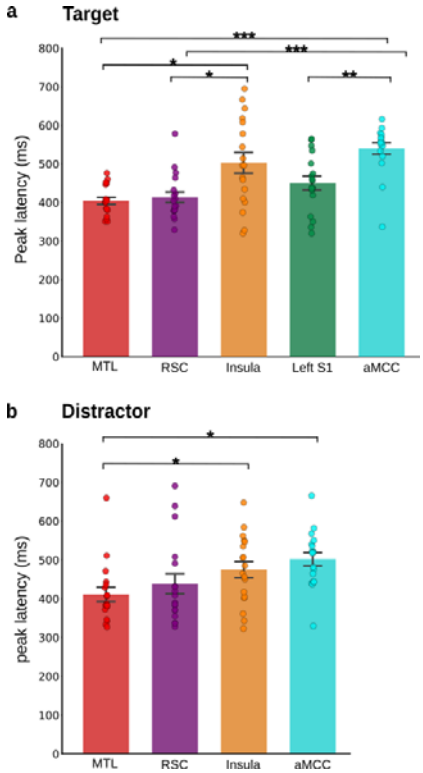

Figure 5: ROIs based M/EEG peak latency analysis for target and distractor. Peak-latency analysis of ROI-based source time courses (mean ± standard error; N=19) for (a) targets and (b) distractors P3. The ROIs include the medial temporal lobe (MTL), retrosplenial cortex (RSC), insula, primary somatosensory cortex (S1), and anterior midcingulate cortex (aMCC). Significant differences between peak latencies for ROIs are indicated by asterisks (* $p < 0.05$, ** $p < 0.01$, *** $p < 0.001$) based on t-tests for repeated measures with Bonferroni correction for multiple comparison.

The M/EEG source time courses were further evaluated in an ROI analysis (Figure 4), including previously established ROIs (Das et al., 2024) in RSC, Insula, S1, and anterior middle cingulate gyrus (aMCC). While RSC and insula were directly adopted, aMCC and S1 from our previous auditory study did not show consistent time courses with the present data. We therefore compared the dSPM maps with the previous S1 ROI and found that the peak of activity was more dorsal in the present data. Accordingly, the ROI used here was shifted more dorsal along the central sulcus. While activity in aMCC was not observed in the current maps within the P3 time window, mapping a later time window (Figure S3) reveals aMCC activity for the present data set as well. However, the activity was overall more anterior compared to the auditory study. The ROI was therefore shifted more anterior for the present analysis to allow us to image the time course of aMCC activity. An ROI in the medial temporal lobe (MTL) was added for this study. This ROI was restricted to the cortex in the sulcus in direct vicinity of the hippocampus (the subiculum) where polarity was consistently positive-going in the maps. Note that the hippocampus itself is not part of the cortical source space in the FreeSurfer parcellation and could therefore not be chosen as an ROI. The source waveforms show P3-like time courses in RSC, MTL, insula and (less prominently) in aMCC. An analysis of the peak latencies for targets (Figure 5a) shows earlier latencies in RSC (414 ± 57 ms) and MTL (404 ± 38 ms), and significantly longer latencies in insula (503 ± 111 ms) and aMCC (540 ± 61 ms; mean ± standard deviation). The response to distractor stimuli also showed long-latency peaks in the P3 range in RSC, insula, MTL, and, less prominently again, in aMCC. Compared to the target P3, however, the response to the distractors is more similar to the standard stimuli in amplitude (Error! Reference source not found.**b**). The latencies of these peaks are in a similar range as for the target P3 (Figure 5b); P3 latencies in standard, midline electrode positions are shown in Figure S4 for comparison.

Next, to estimate the relative contribution of these sources, the MEG sensor and EEG scalp distribution were modeled with a linear combination of these five ROIs. This model was constrained to equal source amplitudes in the left and right hemispheres for each pair of ROIs, with the exception of S1, which was only modeled in the left hemisphere. When this model was applied to the target P3 (Table 1), the strongest weighting was applied to RSC. Activity in insula and S1 was about six times lower and about nine times lower in the MTL. aMCC received only little weight for explaining the P3 peak, unless insula or S1 were removed from the model. Leaving out single sources in this model revealed that RSC explained the most variance in EEG, whereas S1 explained the most variance in MEG. MTL explained only little variance, and insula even less. Matching the overall lower residual variance in EEG compared to MEG, the maps resulting from this simulation are more similar to the original data in EEG than in MEG (Figure 6), although the general distribution can be modeled in both modalities. A similar pattern was observed when the model was applied to the distractor P3 (Table 1).

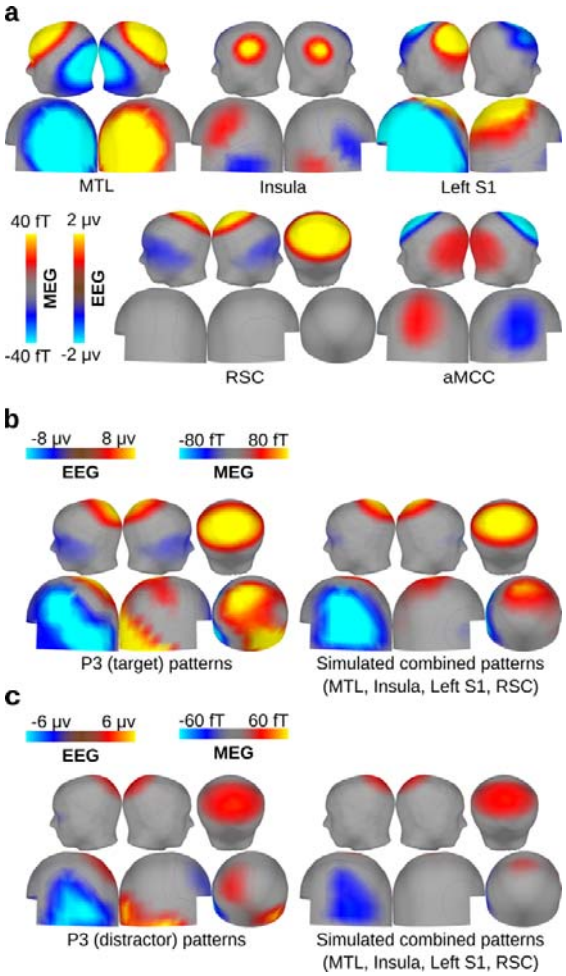

Figure 6: Simulated M/EEG sources and P3 patterns analysis. (a) Spatial pattern of scalp EEG (top) and virtual magnetometer maps (bottom) for MEG, derived from simulated sources (grand average, N=19) in the bilateral medial temporal lobe (MTL), insula, left primary somatosensory cortex (S1), bilateral retrosplenial cortex (RSC), and anterior midcingulate cortex (aMCC). (b, c) Grand-average (N=19) scalp EEG and virtual MEG magnetometer maps at the peak latency for the P3 in Pz (top right) for targets and distractors (bottom right). The combination of simulated sources in MTL, insula, S1, and RSC that best explains the P3 for targets (b, cf. **Table 1**) and distractors (c, cf. **Table 1**).

Table 1: Modelling of the grand-average spatial pattern of target P3 and distractor P3 with simulated M/EEG sources.

Task condition	***Simulated source activation strength (nAm)***					***Residual Variance (%)***	
	Insula	***S1***	***MTL***	***aMCC***	***RSC***	***EEG***	***MEG***
Target P3	***5.50***	***15.50***	***7.0***	***1.25***	***71.25***	***5.89***	***38.29***
	-	*15.25*	*8.50*	*5.0*	*70.50*	*6.16*	*38.16*
	0.0	*-*	*18.50*	*19.25*	*67.75*	*11.72*	*92.38*
	4.75	*16.25*	*-*	*0.0*	*73.75*	*7.39*	*40.48*
	6.50	*15.75*	*6.50*	*-*	*71.50*	*5.81*	*38.40*
	0.0	*14.50*	*15.0*	*9.0*	*-*	*82.80*	*37.66*
Distractor P3	***4.0***	***5.75***	***3.25***	***4.75***	***33.25***	***6.42***	***48.27***
	-	*5.50*	*4.50*	*7.25*	*32.50*	*6.47*	*48.86*
	0.0	*-*	*7.0*	*12.5*	*32.75*	*8.49*	*88.81*
	7.50	*6.0*	*-*	*0.0*	*34.25*	*5.92*	*51.97*
	8.0	*6.25*	*1.0*	*-*	*34.0*	*6.40*	*49.69*
	0.0	*5.75*	*8.75*	*9.75*	*-*	*85.86*	*46.78*

S1, primary somatosensory cortex; MTL, medial temporal lobe; RSC, retro-splenial cortex; aMCC, anterior midcingulate cortex; EEG, electroencephalography; MEG, magnetoencephalography.

To better understand the differential role of sources for MEG and EEG, we performed a separate source analysis of the MEG and EEG data, using the visual target stimuli from the present experiment (Figure 7a) and the auditory target stimuli of a previous experiment (Das et al., 2024); Figure 7b). The results showed that using the EEG, only, revealed overall a similar but somewhat less focused pattern as observed for the combined M/EEG. In contrast, the MEG-only maps showed almost no activity in RSC and only weak activity in the insula (stronger in the auditory data). Only activity in MTL was consistently observed in both MEG and EEG.

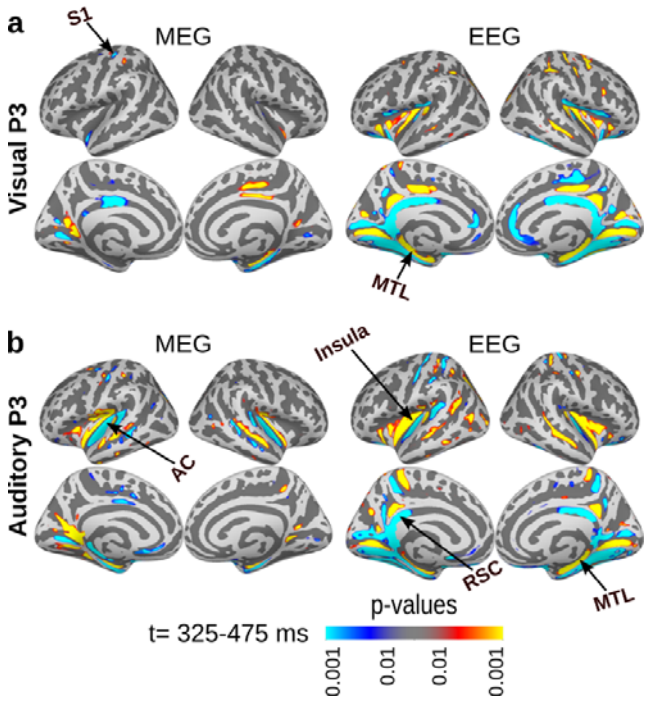

Figure 7: Grand-average dSPM activation maps calculated separately for MEG and EEG. (a) Separate MEG (left) and EEG (right) dSPM maps ($p<0.01$; N=19) for visual target in the time window 325–475 ms after stimulus onset. (b) Separate MEG (left) and EEG (right) dSPM maps ($p<0.01$; N=12) for previously published auditory targets (Das et al., 2024) with the same parameters as used for the visual paradigm in a. Highlighted brain regions include Auditory cortex (AC), medial temporal lobe (MTL), retrosplenial cortex (RSC), primary somatosensory cortex (S1), and insula.

Activity in and around the calcarine fissure was also observed in both MEG and EEG maps, as well as for visual and auditory stimuli alike. However, while the location of this activity was similar for MEG and EEG, the polarity was almost opposite, again with the EEG maps matching better with the combined M/EEG maps. These observations were quite consistent between the visual and auditory oddball paradigms. The most prominent difference between paradigms was the additional presence of surface-negative activity in the auditory cortex when auditory stimuli were used. Auditory cortex activity is more prominent in MEG and comes with a variation of the activity pattern in MTL, which is only observed on detailed inspection. MTL activity in the parahippocampal gyurs in the visual maps is positive in the sulcus and negative on the convexity of the gyrus for the complete extension of the gyrus. In the auditory MEG maps, however, this pattern is only observed in the anterior part of the gyrus, whereas an opposite polarity pattern is mapped to the posterior part of the left parahippocampal gyrus. The latter polarity pattern was previously observed in the time interval of the auditory N1 response and in simulations of surface-negative auditory cortex activity (Das et al., 2024). Together, these data suggest that the auditory MEG maps show a mixture of spread from auditory cortex with activity from a second source in the MTL.

To support the interpretation of the dSPM maps shown so far, we computed simulated M/EEG activity based on single-region, bilateral ROIs (except left S1) and applied dSPM source analysis for MEG and EEG only, as well as combined M/EEG (Figure 8). The simulated MTL activity is similarly mapped in MEG and EEG. However, spread to the calcarine

fissure shows a different pattern in MEG and EEG, which shows high similarity with the pattern observed in the actual P3 maps (Figure 7). The simulation also shows spread to the RSC, but somewhat more anterior than in the P3 maps, leaving out major activity in the PCC. Like the prominent spread to the insula, this is more prominent in EEG compared to MEG. Simulated RSC activity shows comparatively little spread to other areas, but the extension goes quite a bit beyond the ROI, in particular towards the middle cingulate cortex. In EEG, some spread is also observed in the calcarine fissure, with a similar pattern as observed for the MTL simulation. Simulations of insula and aMCC show some spread between ROIs in both directions, which is somewhat unfortunate given their similar response latencies observed in the ROI analysis of the P3. This impression is confirmed by the computational analysis of spread between ROIs (Figures 8b, S5, S6, S7).

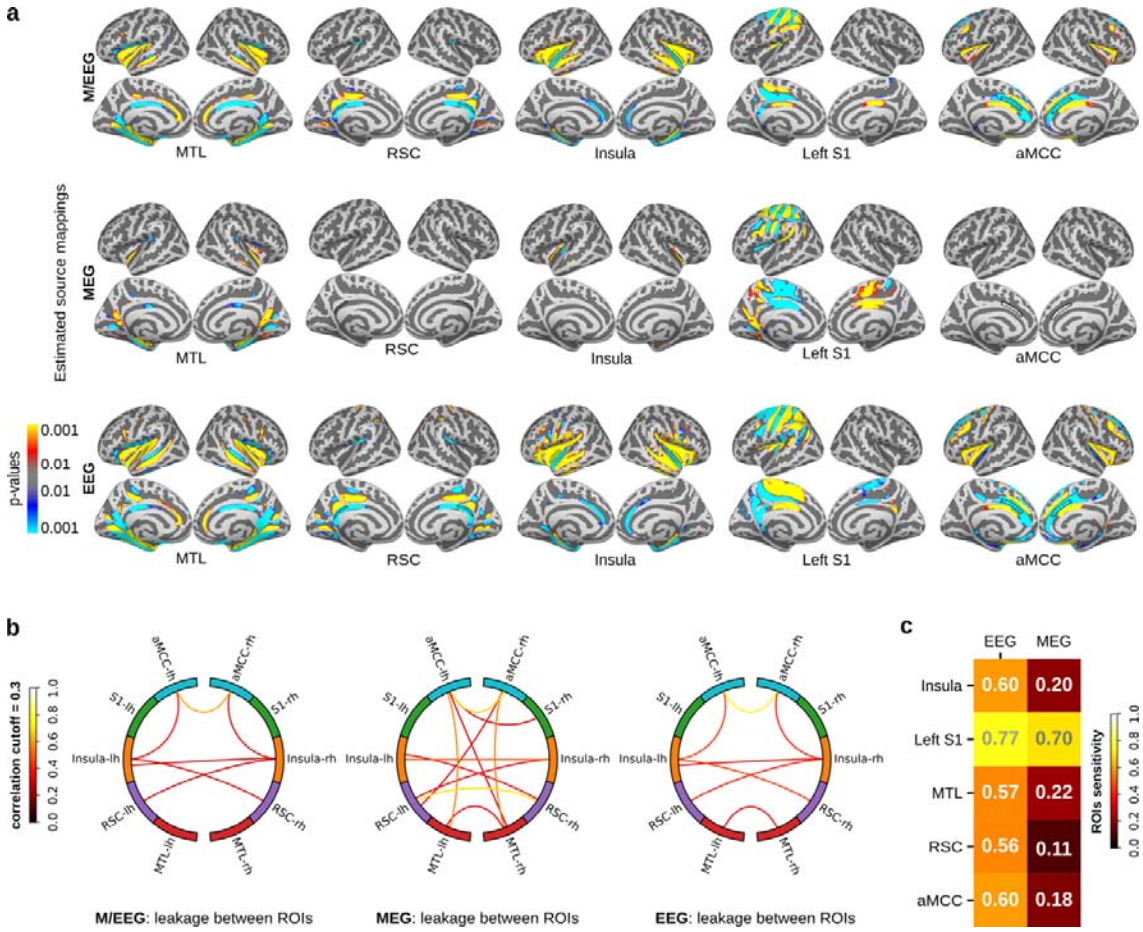

Figure 8: Reconstructed simulated source patterns, spread, and sensitivity analysis for MEG and EEG. (a) Dynamic statistical parametric maps (dSPM) for simulated M/EEG sources (N=19), with a significance threshold of $p < 0.01$. These maps represent simulated sources in the bilateral medial temporal lobe (MTL), bilateral retrosplenial cortex (RSC), bilateral insula, left primary somatosensory cortex (S1), and bilateral anterior midcingulate cortex (aMCC). (b) Point spread analysis for combined M/EEG and separate MEG and EEG data. Each analysis is calculated with individual hemispheric sources (left and right), illustrated with a circular graph, using a correlation cutoff value of 0.3. (c) Sensitivity matrix based on ROIs for EEG and MEG, with sensitivity values ranging from 0 (minimum) to 1 (maximum).

This analysis also suggests considerable spread between RSC and insula, which is not readily observed in the simulated dSPM maps. Finally, the simulation of left-hemisphere S1 activity shows a pattern of left MCC negative and right MCC positive activity in MEG, which was similarly observed in the MEG maps of the P3, suggesting that this can also be classified as spread from S1 in the P3 maps. Finally, we calculated the sensitivity of MEG and EEG for the ROIs used (Figure 8c), ignoring noise. The results show that the strongest asymmetry is observed for the RSC, with a sensitivity of 0.56 in EEG and only 0.11 in MEG. Sensitivity for insula, MTL, and aMCC is similar in EEG, but a factor of two higher in MEG

compared to RSC. By far the strongest sensitivity is observed in S1, which is the only ROI where sensitivity in MEG almost matches EEG.

Discussion

Our results are consistent with the idea that the RSC is the main source of the P3 in EEG (Das et al., 2024). Further support for the RSC comes from a recent study of tone-in-noise detection (Doll et al., 2024), such that a main P3 source in RSC has now been observed with auditory and visual oddball tasks, as well as with a near-threshold, single-tone detection task, providing a reproduction across different paradigms and modalities. While previous experiments all used target stimuli, the detection of which was coupled to a button press, the present data adds a distractor condition without button presses. While the amplitude of this response and, consequently, the signal-to-noise level of the source analysis, were much lower than that of the target-elicited P3, the results are nevertheless similar, suggesting a source in RSC for the distractor-elicited P3 in EEG as well. The detailed comparison of EEG and MEG provided in the present study further shows that the sensitivity of MEG is quite low for an RSC source, implying that other P3 sources are more dominant in MEG.

The most prominent contributor to MEG in the P3 time-window was S1, which in fact should not be considered a component of the P3, because it reflects activity that is clearly time-locked to the button presses in case of the target P3 (Figure S8). Unexpectedly, the multi-source model suggests that S1 activity is also contained in the distractor P3, possibly related to actively suppressed motor responses in these no-go trials (Smith et al., 2008). The other two sources in the focus of this paper are weaker, however, making it more challenging to confirm their role with M/EEG. The presence of P3-like activity in hippocampus is well supported by intracranial EEG (Grunwald et al., 1999; Halgren et al., 1980; McCarthy et al., 1989; Stapleton and Halgren, 1987) and a MTL source has also been suggested based on a series of MEG studies using dipole source analysis (Basile et al., 1997; Rogers et al., 1993; Tarkka et al., 1995). The finding that MTL lesions do not change the P3 in EEG (Johnson, 1988; Onofrj et al., 1992) only pertains to the prominent component at Pz. The latter finding is well explained by our source model, because this activity is mostly generated in RSC. Because MEG is not sensitive to this RSC source, the hippocampal P3 component may appear relatively more prominent in MEG than in EEG. The simulated maximum of an MTL source has been demonstrated to be more frontal in EEG (Figure 4a), and occipital in MEG. The frontal maximum matches well with the EEG scalp distribution suggested for the P3a that was demonstrated to be reduced by unilateral medial temporal lobe lesions (Knight, 1996). If the MTL activity is generated by a hippocampal source, which we argue here, the distinction between P3a and P3b as related to different contexts or stimulus paradigms will require a reevaluation. It is obvious that the hippocampal P3 has been directly recorded with target detection paradigms (Grunwald et al., 1999; Halgren et al., 1980; McCarthy et al., 1989; Stapleton and Halgren, 1987), which are used to obtain the P3b in scalp EEG (Polich, 2007). Based on the data presented in this paper, it appears that the RSC and MTL components of the P3 are present for the target and non-target P3 alike. It is conceivable that the MTL P3 is more prominent in non-target and yet stronger in novelty paradigms (Courchesne et al., 1975; Knight, 1996)(Courchesne et al., 1975; Knight, 1996), shifting the maximum from Pz to Cz (Polich, 2007), or even to Fz(Polich, 2007), or even to Fz. Such a shift of maximum can be easily demonstrated by adding simulated RSC and MTL activity with different relative amplitudes. An overlap of brain areas active for target and non-target stimuli has similarly been observed when target and non-target oddball stimuli were studied in fMRI (Kim, 2014)(Kim, 2014).

A limitation of the source analysis in the present study is that our source space ends at the parahippocampal gyrus and does not include sources in the hippocampus proper, i.e. the cornu Ammonis (CA). Intracranial EEG studies consistently reported negative-going P3 activity for depth electrodes placed along the center of the hippocampal formation, with a maximum in the posterior hippocampus (Grunwald et al., 1999; McCarthy et al., 1989; Stapleton and Halgren, 1987). While these studies also reported contacts in parahippocampal gyrus, no maxima were reported there. We therefore propose that the MTL activity reported in this paper reflects a generator in the CA regions of the hippocampus, rather than in the parahippocampal

gyrus. The orientation of the hippocampal sulcus runs parallel to the hippocampal formation along the medial temporal lobe, predicting a maximum in central or frontal EEG electrodes for sources in posterior subiculum or CA3, because of the orientation of the temporal lobe. The anatomy is more complex in the anterior part of the hippocampus (Iglesias et al., 2015), but the source modeled in the present study was more in posterior MTL in accordance with the intracranial studies (Grunwald et al., 1999; McCarthy et al., 1989; Stapleton and Halgren, 1987). Since the hippocampus is strongly convoluted, it is difficult to estimate the tangential versus radial orientation of a hippocampal P3 source, but provided our source analysis, it is expected to have a strong tangential component, suggesting a source in the upper part of the hippocampus, which comprises area CA3 (Sämann et al., 2022). These sources are only a few millimeters away from our ROI in the hippocampal sulcus, which is why we think that the MTL ROI used here serves as a reasonable proxy for a real hippocampus source. Since this source also receives spread from auditory cortex (Das et al., 2024), it is more difficult to track with auditory stimuli. The present visual study, however, almost certainly rules out that the activity we observed in MTL could be spread from the auditory cortex. For a proof-of-principle analysis, we added an additional source space for the hippocampus proper, including regions CA1 - 3, to the whole cortical source space of a single data set (Figure 9). Mapping the P3 with this extended source space shows similar time courses for the subiculum and CA, but with negative-going polarity in CA. These preliminary results support both assumptions made in the paragraph above. First, that the subiculum ROI can be used as a proxy to measure activity that is more likely generated in the CA regions of the hippocampus, and second, that this activity is negative at the inner (cortical) surface of the hippocampus.

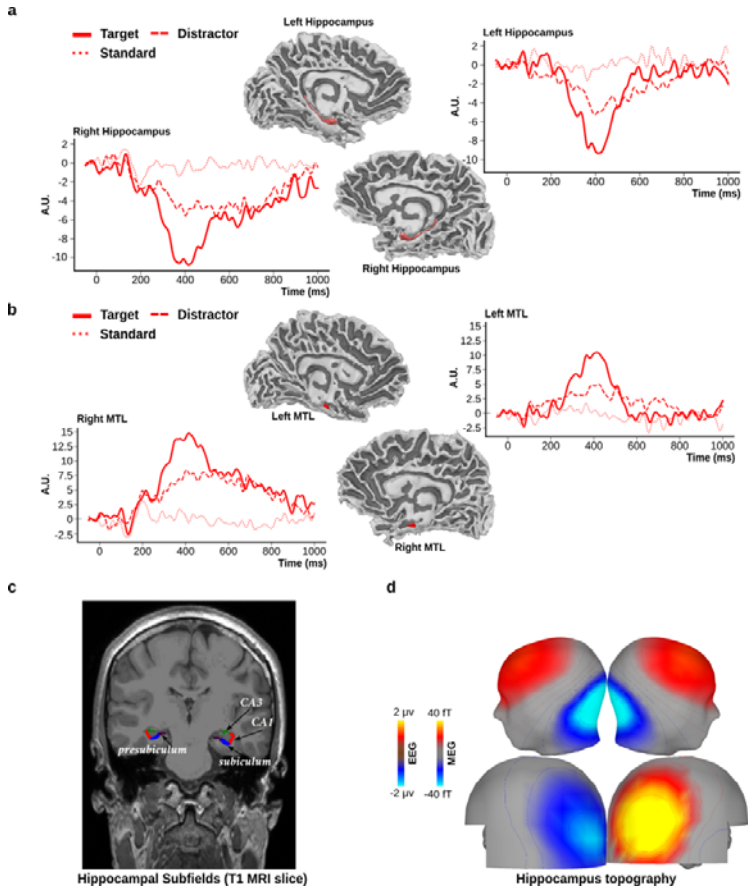

Figure 9: Comparison of hippocampal and parahippocampal sources in a single participant with good signal quality. (a) Source activity in the left and right hippocampus for targets (solid), distractors (dashed), and standards (dotted). For this analysis a distributed source space in the cornu ammonis (CA) regions CA1-3 was added to the cortical source space (indicated in red in the 3D brain). (b) Source activity based on the MTL ROI used in the main analysis for the same participant. Only part of the ROI (red) can be seen because the rest is buried in the depth of the fissure. (c) Parcellation of the hippocampal structures for the same participant in a coronal section with the pre-subiculum (lilac), subiculum (blue), CA1 (red),

and CA (3) (green). CA2 is not segregated from CA1 and 3. As can be seen here, the surface of the subiculum (which mostly coincides with the MTL ROI used in the main analysis) is opposite to CA, and in particular to CA3. As a consequence, the waveform polarity is negative at the cortical surface for the hippocampus (CA, panel a) and positive for the MTL ROI (subiculum, panel b). (d) Simulated EEG and MEG distribution for the same data set based on negative-going activity in CA. Note the similarity to the MTL simulation in Figure 6a.

There has been a long discussion on whether deep sources like the hippocampus can be recorded in MEG at all. The resolution to this question appears to be highly individual: Some subcortical sources like the auditory brainstem response can be recorded with MEG (Dykstra et al., 2016; Parkkonen et al., 2009) and are clearly identified not only by their source location but also by their early latency. No significant difference has been found for the sensitivity of magnetometers and gradiometers for deep sources (Hunold et al., 2016). Generally, the problem for MEG compared to EEG is not only the stronger signal drop with depth for tangential sources, but also its lack of sensitivity to radial sources (Hämäläinen et al., 1993). This is well illustrated in case of the RSC, where our simulations demonstrate the strong discrepancy in sensitivity between MEG and EEG. For the MTL, in comparison, sensitivity was not so much stronger for EEG compared to MEG in our simulation. We cannot yet provide a simulation estimate for the CA regions of the hippocampus, such that our simulations in this paper rely on the posterior subiculum. Signals from hippocampus are expected to be more attenuated in comparison to the subiculum, because of the higher curvature and associated cancelation (Shaw et al., 2013), applying similarly to EEG and MEG. Methodological studies incorporating this curvature still support that the hippocampus proper (i.e. CA1-3) can be recorded with MEG (Attal and Schwartz, 2013; Krishnaswamy et al., 2017; Pizzo et al., 2019; Ruzich et al., 2019). Further empirical evidence to support these considerations comes from a series of studies that demonstrated that MTL sources of hippocampal replay can be consistently recorded with MEG (Liu et al., 2019; Wimmer et al., 2020).

One obstacle in the interpretation of the P3 dSPM maps is the consistent observation of activity in the calcarine fissure, which was observed in MEG and EEG with both visual and auditory oddball paradigms. Two details lead us to suggest that this calcarine pattern in the P3 time window is spread rather than correctly located source activity. First, the polarity of the pattern is opposite in MEG- and EEG-only analyses, which is difficult to explain for a source generated directly in primary visual cortex. Second, the same pattern is observed when MTL activity is simulated and then mapped with the same source analysis technique, suggesting that the calcarine pattern observed in the dSPM maps may simply be spread from a hippocampal source, and, to a lesser degree, from RSC. Still, this observation remains incompletely understood because, in some cases, activity in the calcarine fissure appeared to be stronger than in MTL.

The other problem that cannot be resolved completely is the spread between regions that we think are all generators of the P3 in M/EEG. This includes, but is not limited to, spread between MTL and insula, as well as between insula and aMCC. In the case of the insula, intracranial recordings have confirmed insular activity in the P3 latency range (Citherlet et al., 2020). We therefore think that, despite the interaction with other sources, an insular source of the P3 is quite likely as well. As for the MTL source, the present data are important for this conclusion, because another source of spread to the insula was the auditory cortex (Das et al., 2024), which has been avoided in the present study. One detail of the insular P3 that remains unclear is its polarity at the cortical surface. Based on the RSC model, the main generator of the P3 is negative-going at the cortical surface, as is the aMCC source. The same is to be expected for the hippocampal source, based on the considerations discussed above and with respect to the intracranial studies (Grunwald et al., 1999; Halgren et al., 1980; Stapleton and Halgren, 1987). However, the insula ROI used here and in our previous auditory study (Das et al., 2024) shows positive-going polarity at the cortical surface, which is rather unlikely if the different P3 components reflected a similar cortical process. One possibility could be that we chose the wrong side of a sulcus/gyrus in our attempt to define an ROI of homogeneous polarity. Overall, activity in the insula appeared to be more positive-going, but this aspect of the source model will require further evaluation. The available intracranial data do not answer this question, as far as we can tell (Citherlet et al., 2020).

Beyond the question of P3 sources, which was the main focus of this paper and awaits confirmation from future work, another important question is what these sources indicate about the role in human cognition that the P3 indexes. Based on the

peak latency of the sources, we found that hippocampus and RSC on the one hand, and insula and aMCC, on the other hand, have similar peak latencies. The first of these pairs, the RSC and hippocampus, have been shown to be densely and reciprocally connected (Kobayashi and Amaral, 2007, 2003). Traditionally, RSC and hippocampus have been thought to be jointly involved in episodic memory encoding and spatial navigation (Vann et al., 2009). The RSC is also thought to be generally involved in the coding of significant events (Smith et al., 2018) which may be more closely related to the P3 and consistent with the presence of RSC and hippocampal P3 activity for both target and non-target events. The second pair, aMCC and insular cortex, are frequently coactivated during resting-state fMRI activity and are variably labeled as the ventral attention (Menon and Uddin, 2010; Thomas Yeo et al., 2011) or cingulo-opercular network (Coste and Kleinschmidt, 2016). While RSC and hippocampal activity build up towards the button press and then decrease again, the maximum activity in aMCC showed a longer latency after the button press. The insular latency observed in the present visual study was longer than in RSC/MTL and numerically earlier, but not significantly different from aMCC. This is further evident when source time-courses were computed for targets, averaged by the button press (Figure S8b). Note, however, that insula activity was somewhat earlier in the previous auditory study (Das et al., 2024), suggesting overall that aMCC activity may succeed insular activity in latency. Studying P3 at the source level instead of the sensor level in future studies may help to understand the functional anatomy of P3 for human cognition.

Limitations

The source analysis techniques applied in the present study have inherent limitations because of the non-unique solution of the inverse problem in a volume conductor(Hämäläinen et al., 1993). While techniques that do not have such limitation, like fMRI and iEEG, support the sources in RSC (Das et al., 2024), hippocampus (Grunwald et al., 1999; McCarthy et al., 1989; Stapleton and Halgren, 1987), and insula (Citherlet et al., 2020), we cannot exclude that further sources contribute to the P3. A number of such sources have been suggested based on fMRI and iEEG (Bledowski et al., 2004; Halgren et al., 1995b, 1995a; Mulert et al., 2004) but were not observed in our source analysis based on M/EEG. Alternative source configurations can therefore not be ruled out at this point. For example, it is possible that the contribution of other sources is more variable across participants and is therefore not observed in the group-level analysis used in the present study. Also, the spatial precision of M/EEG is limited, such that the exact location of the sources suggested here should be interpreted cautiously and considering that M/EEG cannot estimate the extend of a source. As has been extensively discussed above, the source space used for the group-level analysis does not yet include the CA regions of the hippocampus proper. While we think that the subiculum can be used as a proxy for posterior hippocampus for now, it is desirable to add the CA regions to the cortical source space on the long run. Finally, the analysis of the distractor P3 in the present study was only exploratory and will therefore require confirmatory studies to probe the source configuration for the P3a and P3b variants proposed above.

Author contributions

Diptyajit Das: Conceptualization, Experimental design, Data curation, Investigation, Methodology, Formal analysis, Visualization, Writing - original draft & editing.

Matti S. Hämäläinen: Methodology, Validation, Writing - reviewing & editing.

Andrew R. Dykstra: Validation, Writing - reviewing & editing.

Andre Rupp: Validation, Writing - reviewing & editing.

Alexander Gutschalk: Conceptualization, Experimental design, Methodology, Validation, Writing - original draft & editing, Funding acquisition, Supervision.

Data availability

The raw and processed MEG and EEG data and scripts will be shared upon publication and can be accessed on heiDATA, the open research data repository of Heidelberg University, Germany.

Declaration of interest

None of the authors have potential conflicts of interest to be disclosed.

Acknowledgements

This work was supported by Deutsche Forschungsgemeinschaft grant DFG 593/5-1 (AG) and by National Institute of Neurological Disorders and Stroke (NIH) grant 7R01NS104585 (MSH).

References

Attal, Y., Schwartz, D., 2013. Assessment of Subcortical Source Localization Using Deep Brain Activity Imaging Model with Minimum Norm Operators: A MEG Study. PLoS One 8. https://doi.org/10.1371/journal.pone.0059856

Basile, L.F.H., Rogers, R.L., Simos, P.G., Papanicolaou, A.C., 1997. Magnetoencephalographic evidence for common sources of long latency fields to rare target and rare novel visual stimuli. International Journal of Psychophysiology 25, 123–137. https://doi.org/10.1016/S0167-8760(96)00715-5

Bledowski, C., Prvulovic, D., Hoechstetter, K., Scherg, M., Wibral, M., Goebel, R., Linden, D.E.J., 2004. Localizing P300 generators in visual target and distractor processing: A combined event-related potential and functional magnetic resonance imaging study, in: Journal of Neuroscience. pp. 9353–9360. https://doi.org/10.1523/JNEUROSCI.1897-04.2004

Citherlet, D., Boucher, O., Tremblay, J., Robert, M., Gallagher, A., Bouthillier, A., Lepore, F., Nguyen, D.K., 2020. Spatiotemporal dynamics of auditory information processing in the insular cortex: an intracranial EEG study using an oddball paradigm. Brain Struct Funct 225, 1537–1559. https://doi.org/10.1007/s00429-020-02072-z

Coste, C.P., Kleinschmidt, A., 2016. Cingulo-opercular network activity maintains alertness. Neuroimage 128, 264–272. https://doi.org/10.1016/j.neuroimage.2016.01.026

Courchesne, E., Hillyard, S.A., Galambos, R., 1975. Stimulus novelty, task relevance and the visual evoked potential in man. Electroencephalogr Clin Neurophysiol 39, 131–143. https://doi.org/10.1016/0013-4694(75)90003-6

Dale, A.M., Fischl, B., Sereno, M.I., 1999. Cortical Surface-Based Analysis. Neuroimage 9, 179–194. https://doi.org/10.1006/nimg.1998.0395

Dale, A.M., Liu, A.K., Fischl, B.R., Buckner, R.L., Belliveau, J.W., Lewine, J.D., Halgren, E., 2000. Dynamic Statistical Parametric Mapping. Neuron 26, 55–67. https://doi.org/10.1016/S0896-6273(00)81138-1

Das, D., Shaw, M.E., Hämäläinen, M.S., Dykstra, A.R., Doll, L., Gutschalk, A., 2024. A role for retro-splenial cortex in the task-related P3 network. Clinical Neurophysiology 157, 96–109. https://doi.org/10.1016/j.clinph.2023.11.014

Doll, L., Dykstra, A.R., Gutschalk, A., 2024. Perceptual awareness of near-threshold tones scales gradually with auditory cortex activity and pupil dilation. iScience 110530. https://doi.org/10.1016/j.isci.2024.110530

Dykstra, A.R., Burchard, D., Starzynski, C., Riedel, H., Rupp, A., Gutschalk, A., 2016. Lateralization and Binaural Interaction of Middle-Latency and Late-Brainstem Components of the Auditory Evoked Response. JARO - Journal of the Association for Research in Otolaryngology 17, 357–370. https://doi.org/10.1007/s10162-016-0572-x

Engemann, D.A., Gramfort, A., 2015. Automated model selection in covariance estimation and spatial whitening of MEG and EEG signals. Neuroimage 108, 328–342. https://doi.org/10.1016/j.neuroimage.2014.12.040

Fischl, B., 2012. FreeSurfer. Neuroimage 62, 774–781. https://doi.org/10.1016/j.neuroimage.2012.01.021

Glasser, M.F., Coalson, T.S., Robinson, E.C., Hacker, C.D., Harwell, J., Yacoub, E., Ugurbil, K., Andersson, J., Beckmann, C.F., Jenkinson, M., Smith, S.M., Van Essen, D.C., 2016. A multi-modal parcellation of human cerebral cortex. Nature 536, 171–178. https://doi.org/10.1038/nature18933

Gramfort, A., 2013. MEG and EEG data analysis with MNE-Python. Front Neurosci 7. https://doi.org/10.3389/fnins.2013.00267

Grunwald, T., Beck, H., Lehnertz, K., Blümcke, I., Pezer, N., Kutas, M., Kurthen, M., Karakas, H.M., Van Roost, D., Wiestler, O.D., Elger, C.E., 1999. Limbic P300s in temporal lobe epilepsy with and without Ammon's horn sclerosis. European Journal of Neuroscience 11, 1899–1906. https://doi.org/10.1046/j.1460-9568.1999.00613.x

Halgren, E., Baudena, P., Clarke, J.M., Heit, G., Li6geois, C., Chauvel, P., Musolino, A., 1995a. Intracerebral potentials to rare target and distractor auditory and visual stimuli. I. Superior temporal plane and parietal lobe, Electroencephalography and clinical Neurophysiology.

Halgren, E., Baudena, P., Clarke, J.M., Heit, G., Marinkovic, K., Devaux, B., Vignal, J.-P., Biraben, A., 1995b. Intracerebral potentials to rare target and distractor auditory and visual stimuli. II. Medial, lateral and posterior temporal lobe. Electroencephalogr Clin Neurophysiol 94, 229–250. https://doi.org/10.1016/0013-4694(95)98475-N

Halgren, E., Squires, N.K., Wilson, C.L., Rohrbaugh, J.W., Babb, T.L., Crandall, P.H., 1980. Endogenous Potentials Generated in the Human Hippocampal Formation and Amygdala by Infrequent Events. Science (1979) 210, 803–805. https://doi.org/10.1126/science.7434000

Hämäläinen, M., Hari, R., Ilmoniemi, R.J., Knuutila, J., Lounasmaa, O. V., 1993. Magnetoencephalography—theory, instrumentation, and applications to noninvasive studies of the working human brain. Rev Mod Phys 65, 413–497. https://doi.org/10.1103/RevModPhys.65.413

Hämäläinen, M.S., Ilmoniemi, R.J., 1994. Interpreting magnetic fields of the brain: minimum norm estimates. Med Biol Eng Comput 32, 35–42. https://doi.org/10.1007/BF02512476

Hamalainen, M.S., Sarvas, J., 1989. Realistic conductivity geometry model of the human head for interpretation of neuromagnetic data. IEEE Trans Biomed Eng 36, 165–171. https://doi.org/10.1109/10.16463

Haufe, S., Meinecke, F., Görgen, K., Dähne, S., Haynes, J.-D., Blankertz, B., Bießmann, F., 2014. On the interpretation of weight vectors of linear models in multivariate neuroimaging. Neuroimage 87, 96–110. https://doi.org/10.1016/j.neuroimage.2013.10.067

Hauk, O., Stenroos, M., Treder, M.S., 2022. Towards an objective evaluation of EEG/MEG source estimation methods – The linear approach. Neuroimage 255. https://doi.org/10.1016/j.neuroimage.2022.119177

Hillyard, S.A., Squires, K.C., Bauer, J.W., Lindsay, P.H., 1971. Evoked Potential Correlates of Auditory Signal Detection. Science (1979) 172, 1357–1360. https://doi.org/10.1126/science.172.3990.1357

Hunold, A., Funke, M.E., Eichardt, R., Stenroos, M., Haueisen, J., 2016. EEG and MEG: sensitivity to epileptic spike activity as function of source orientation and depth. Physiol. Meas. 37, 1146-1162.

Hyvarinen, A., 1999. Fast and robust fixed-point algorithms for independent component analysis. IEEE Trans Neural Netw 10, 626–634. https://doi.org/10.1109/72.761722

Iglesias, J.E., Augustinack, J.C., Nguyen, K., Player, C.M., Player, A., Wright, M., Roy, N., Frosch, M.P., McKee, A.C., Wald, L.L., Fischl, B., Van Leemput, K., 2015. A computational atlas of the hippocampal formation using ex vivo, ultra-high resolution MRI: Application to adaptive segmentation of in vivo MRI. Neuroimage 115, 117–137. https://doi.org/10.1016/j.neuroimage.2015.04.042

Jas, M., Engemann, D.A., Bekhti, Y., Raimondo, F., Gramfort, A., 2017. Autoreject: Automated artifact rejection for MEG and EEG data. Neuroimage 159, 417–429. https://doi.org/10.1016/j.neuroimage.2017.06.030

Johnson, R., 1988. SCALP-RECORDED P300 ACTIVITY IN PATIENTS FOLLOWING UNILATERAL TEMPORAL LOBECTOMY. Brain 111, 1517–1529. https://doi.org/10.1093/brain/111.6.1517

Kim, H., 2014. Involvement of the dorsal and ventral attention networks in oddball stimulus processing: A meta-analysis. Hum Brain Mapp 35, 2265–2284. https://doi.org/10.1002/hbm.22326

Knight, R.T., 1996. Contribution of human hippocampal region to novelty detection. Nature 383, 256–259. https://doi.org/10.1038/383256a0

Kobayashi, Y., Amaral, D.G., 2007. Macaque monkey retrosplenial cortex: III. Cortical efferents. Journal of Comparative Neurology 502, 810–833. https://doi.org/10.1002/cne.21346

Kobayashi, Y., Amaral, D.G., 2003. Macaque monkey retrosplenial cortex: II. Cortical afferents. Journal of Comparative Neurology 466, 48–79. https://doi.org/10.1002/cne.10883

Kretzschmar, B., Gutschalk, A., 2010. A sustained deviance response evoked by the auditory oddball paradigm. Clinical Neurophysiology 121, 524–532. https://doi.org/10.1016/j.clinph.2009.11.088

Krishnaswamy, P., Obregon-Henao, G., Ahveninen, J., Khan, S., Babadi, B., Iglesias, J.E., Hämäläinen, M.S., Purdon, P.L., 2017. Sparsity enables estimation of both subcortical and cortical activity from MEG and EEG. Proc Natl Acad Sci U S A 114, E10465–E10474. https://doi.org/10.1073/pnas.1705414114

Larson, E., Taulu, S., 2018. Reducing Sensor Noise in MEG and EEG Recordings Using Oversampled Temporal Projection. IEEE Trans Biomed Eng 65, 1002–1013. https://doi.org/10.1109/TBME.2017.2734641

Lin, F., Belliveau, J.W., Dale, A.M., Hämäläinen, M.S., 2006. Distributed current estimates using cortical orientation constraints. Hum Brain Mapp 27, 1–13. https://doi.org/10.1002/hbm.20155

Liu, Y., Dolan, R.J., Kurth-Nelson, Z., Behrens, T.E.J., 2019. Human Replay Spontaneously Reorganizes Experience. Cell 178, 640-652.e14. https://doi.org/10.1016/j.cell.2019.06.012

McCarthy, G., Wood, C., Williamson, P., Spencer, D., 1989. Task-dependent field potentials in human hippocampal formation. The Journal of Neuroscience 9, 4253–4268. https://doi.org/10.1523/JNEUROSCI.09-12-04253.1989

Menon, V., Uddin, L.Q., 2010. Saliency, switching, attention and control: a network model of insula function. Brain Struct Funct 214, 655–667. https://doi.org/10.1007/s00429-010-0262-0

Molins, A., Stufflebeam, S.M., Brown, E.N., Hämäläinen, M.S., 2008. Quantification of the benefit from integrating MEG and EEG data in minimum ℓ2-norm estimation. Neuroimage 42, 1069–1077. https://doi.org/10.1016/j.neuroimage.2008.05.064

Mulert, C., Pogarell, O., Juckel, G., Rujescu, D., Giegling, I., Rupp, D., Mavrogiorgou, P., Bussfeld, P., Gallinat, J., Möller, H.J., Hegerl, U., 2004. The neural basis of the P300 potential. European Archives of Psychiatry and Clinical Neurosciences 254. https://doi.org/10.1007/s00406-004-0469-2

Onofrj, M., Fulgente, T., Nobilio, D., Malatesta, G., Bazzano, S., Colamartino, P., Gambi, D., 1992. P3 recordings in patients with bilateral temporal lobe lesions. Neurology 42, 1762–7. https://doi.org/10.1212/wnl.42.9.1762

Parkkonen, L., Fujiki, N., Mäkelä, J.P., 2009. Sources of auditory brainstem responses revisited: Contribution by magnetoencephalography. Hum Brain Mapp 30, 1772–1782. https://doi.org/10.1002/hbm.20788

Perrin, F., Pernier, J., Bertrand, O., Echallier, J.F., 1989. Spherical splines for scalp potential and current density mapping, Electroencephalography and clinical Neurophysiology.

Pizzo, F., Roehri, N., Medina Villalon, S., Trébuchon, A., Chen, S., Lagarde, S., Carron, R., Gavaret, M., Giusiano, B., McGonigal, A., Bartolomei, F., Badier, J.M., Bénar, C.G., 2019. Deep brain activities can be detected with magnetoencephalography. Nat Commun 10. https://doi.org/10.1038/s41467-019-08665-5

Polich, J., 2007. Updating P300: An integrative theory of P3a and P3b. Clinical Neurophysiology. https://doi.org/10.1016/j.clinph.2007.04.019

Rogers, R.L., Basile, L.F., Papanicolaou, A.C., Eisenberg, H.M., 1993. Magnetoencephalography reveals two distinct sources associated with late positive evoked potentials during visual oddball task. Cereb Cortex 3, 163–9. https://doi.org/10.1093/cercor/3.2.163

Ruzich, E., Crespo-García, M., Dalal, S.S., Schneiderman, J.F., 2019. Characterizing hippocampal dynamics with MEG: A systematic review and evidence-based guidelines. Hum Brain Mapp. https://doi.org/10.1002/hbm.24445

Sämann, P.G., Iglesias, J.E., Gutman, B., Grotegerd, D., Leenings, R., Flint, C., Dannlowski, U., Clarke-Rubright, E.K., Morey, R.A., van Erp, T.G.M., Whelan, C.D., Han, L.K.M., van Velzen, L.S., Cao, B., Augustinack, J.C., Thompson, P.M., Jahanshad, N., Schmaal, L., 2022. FreeSurfer-based segmentation of hippocampal subfields: A review of methods and applications, with a novel quality control procedure for ENIGMA studies and other collaborative efforts. Hum Brain Mapp. https://doi.org/10.1002/hbm.25326

Sarvas, J., 1987. Basic mathematical and electromagnetic concepts of the biomagnetic inverse problem. Phys Med Biol 32, 11–22. https://doi.org/10.1088/0031-9155/32/1/004

Shaw, M.E., Hämäläinen, M.S., Gutschalk, A., 2013. How anatomical asymmetry of human auditory cortex can lead to a rightward bias in auditory evoked fields. Neuroimage 74, 22–29. https://doi.org/10.1016/j.neuroimage.2013.02.002

Smith, D.M., Miller, A.M.P., Vedder, L.C., 2018. The retrosplenial cortical role in encoding behaviorally significant cues. Behavioral Neuroscience 132, 356–365. https://doi.org/10.1037/bne0000257

Smith, J.L., Johnstone, S.J., Barry, R.J., 2008. Movement-related potentials in the Go/NoGo task: The P3 reflects both cognitive and motor inhibition. Clinical Neurophysiology 119, 704–714. https://doi.org/10.1016/j.clinph.2007.11.042

Squires, N.K., Squires, K.C., Hillyard, S.A., 1975. Two varieties of long-latency positive waves evoked by unpredictable auditory stimuli in man. Electroencephalogr Clin Neurophysiol 38, 387–401. https://doi.org/10.1016/0013-4694(75)90263-1

Stapleton, J.M., Halgren, E., 1987. Endogenous potentials evoked in simple cognitive tasks: depth components and task correlates. Electroencephalogr Clin Neurophysiol 67, 44–52. https://doi.org/10.1016/0013-4694(87)90162-3

Tarkka, I.M., Stokić, D.S., Basile, L.F., Papanicolaou, A.C., 1995. Electric source localization of the auditory P300 agrees with magnetic source localization. Electroencephalogr Clin Neurophysiol 96, 538–45. https://doi.org/10.1016/0013-4694(95)00087-f

Thomas Yeo, B.T., Krienen, F.M., Sepulcre, J., Sabuncu, M.R., Lashkari, D., Hollinshead, M., Roffman, J.L., Smoller, J.W., Zöllei, L., Polimeni, J.R., Fischl, B., Liu, H., Buckner, R.L., 2011. The organization of the human cerebral cortex estimated by intrinsic functional connectivity. J Neurophysiol 106, 1125–1165. https://doi.org/10.1152/jn.00338.2011

Uutela, K., Taulu, S., Hämäläinen, M., 2001. Detecting and Correcting for Head Movements in Neuromagnetic Measurements. Neuroimage 14, 1424–1431. https://doi.org/10.1006/nimg.2001.0915

Vann, S.D., Aggleton, J.P., Maguire, E.A., 2009. What does the retrosplenial cortex do? Nat Rev Neurosci 10, 792–802. https://doi.org/10.1038/nrn2733

Verleger, R., 2020. Effects of relevance and response frequency on P3b amplitudes: Review of findings and comparison of hypotheses about the process reflected by P3b. Psychophysiology 57. https://doi.org/10.1111/psyp.13542

Wimmer, G.E., Liu, Y., Vehar, N., Behrens, T.E.J., Dolan, R.J., 2020. Episodic memory retrieval success is associated with rapid replay of episode content. Nat Neurosci 23, 1025–1033. https://doi.org/10.1038/s41593-020-0649-z